



HAL
open science

Effect of reduction on Co catalyst active phase highlighted by an original approach coupling ASAXS and electron tomography

S. Humbert, G. Desjouis, T. Bizien, L. Lemaitre, Ahmed Taleb, C. Dalverny,
L. Sorbier, A S Gay

► To cite this version:

S. Humbert, G. Desjouis, T. Bizien, L. Lemaitre, Ahmed Taleb, et al.. Effect of reduction on Co catalyst active phase highlighted by an original approach coupling ASAXS and electron tomography. Journal of Catalysis, 2018, 366, pp.202-212. 10.1016/j.jcat.2018.07.024 . hal-01980505

HAL Id: hal-01980505

<https://ifp.hal.science/hal-01980505>

Submitted on 14 Jan 2019

HAL is a multi-disciplinary open access archive for the deposit and dissemination of scientific research documents, whether they are published or not. The documents may come from teaching and research institutions in France or abroad, or from public or private research centers.

L'archive ouverte pluridisciplinaire **HAL**, est destinée au dépôt et à la diffusion de documents scientifiques de niveau recherche, publiés ou non, émanant des établissements d'enseignement et de recherche français ou étrangers, des laboratoires publics ou privés.

Effect of reduction on Co catalyst active phase highlighted by an original approach coupling ASAXS and electron tomography

S. Humbert^a, G. Desjouis^a, T. Bizien^b, L. Lemaitre^a, AL Taleb^a, C. Dalverny^c, L. Sorbier^a, AS Gay^a

^a*IFP Energies nouvelles, Rond-point de l'échangeur de Solaize, BP 3, 69360 Solaize, France*

^b*SOLEIL Synchrotron, L'Orme des Merisiers, Gif-Sur-Yvette, 91192 Saint-Aubin, France*

^c*CTμ, Université Claude Bernard Lyon1, 5 rue Raphael Dubois, 69622 Villeurbanne Cedex, France*

Abstract

Diversification of liquid fuel sources for transportation plays a key role in the energetic transition. High quality and clean diesels can be produced by Fischer-Tropsch synthesis, which interest is renewed in as much it can be performed from syngas (CO+H₂) produced by conversion of natural gas or gasification of lignocellulosic biomass, leading, in this latter case, to fuels from renewable resource. Catalytic performance (activity and selectivity) of cobalt-based catalysts are related to the physico-chemical characteristics of the cobalt nanoparticles. The present study propose a new approach to obtain a detailed and exhaustive description of the cobalt active phase in FT catalysts. We combined Anomalous Small Xray Scattering (ASAXS) and electron tomography, giving complementary insights on the microstructure and size distribution of both cobalt nanoparticles and aggregates. This approach, carried out on a cobalt/alumina-silica catalysts studied first at the oxide state and then at the reduced state, allowed to highlight the mechanisms involved at the nanoscale during the reduction step. Reduction impact is significant on aggregates morphology, causing their fragmentation and increasing their accessibility. As a perspective, a better knowledge of cobalt aggregates morphology will help to understand their impact on the catalyst performance.

Keywords

Cobalt, catalyst, Fischer-Tropsch, electron tomography, TEM, ASAXS, nanoparticles

32 **1 Introduction**

33 Diversification of liquid fuel sources for transportation plays a key role in the energetic transition.
34 Fischer-Tropsch Synthesis (FTS), initially devoted to convert coal into fuels, has become attractive as it
35 can be performed from syngas ($\text{CO}+\text{H}_2$) produced by gasification of lignocellulosic biomass, leading, in
36 this latter case, to fuels from renewable resource [1][2]. Low-temperature FTS, based on cobalt catalysts,
37 produces long-chain hydrocarbons leading, after upgrading, to high quality and clean diesels [1][3] [4].
38 Catalytic performance (activity and selectivity) of Fischer-Tropsch catalysts is related to the physico-
39 chemical characteristics of the Co nanoparticles. In particular, for all studied supports (carbon nanofibers,
40 γ -alumina), authors observe a rapid increase of the catalytic activity when the cobalt particle size
41 increases to a certain diameter and, then, the activity decreases with further increase in particle size
42 showing a volcano shape curve in catalytic activity. Besides, the C_5^+ selectivity is also known to be
43 related to the size of the nanoparticles and increases while increasing the size of the particles, to circa
44 fifteen nanometers. Depending of the support, the optimal size for higher activity and selectivity is
45 between 6 and 9 nm [5] [6] [7], smaller particles leading to a significant activity loss. From these results,
46 it is crucial to characterize the nanoparticles, specially their size, which is unlikely to be monodisperse.
47 However, in high-loaded cobalt catalysts (up to 15 wt % Co), the nanoparticles are usually not uniformly
48 dispersed and aggregation of cobalt nanoparticles is often observed, forming aggregates of tens to
49 thousands of nanometers [8] [9]. However, the impact of Co aggregation on activity and selectivity is still
50 unclear / debated. Munnik et al. [8] [9] have observed that the aggregates present in high-loaded catalysts
51 supported on silica were formed during the drying process, after impregnation of aqueous cobalt nitrate
52 precursors. Thus controlling the drying temperature will allow a decrease in aggregate formation rate. By
53 studying catalysts prepared in order to vary the aggregation rate [8], they related an increase of C_5^+
54 selectivity with the increase of the aggregates size.

55 Basing on this literature, it seems essential to characterize both nanoparticle and aggregate scales to fully
56 understand and explain the catalytic performance of the high-loaded cobalt catalysts.

57 For this purpose, a complete description of the active phase implies measuring i) the size distribution of
58 the isolated nanoparticles, ii) the proportion of Co involved in aggregates or in individual particles, iii)
59 the size of the aggregates and iv) the microstructure of aggregates that controls the accessibility of
60 reactant and product within the aggregates. These steps are essential to calculate the intrinsic activity and
61 selectivity and evaluate the impact of aggregation independently to other parameters such as the particles
62 size and the support effect.

63 Several complementary techniques are commonly used to characterize the Co active phase in FTS
64 catalysts. In particular, Co dispersion is measured by H₂ chemisorption, the mean oxide crystallites size is
65 usually measured by X-ray diffraction (XRD) [10] and the particles and aggregates size distribution can
66 be measured by techniques based on transmission electron microscopy (TEM), such as dark-field TEM or
67 HAADF-STEM (high angle annular dark field-scanning transmission electron microscopy) [6,8,9,11].
68 Concerning the XRD technique, it provides a good evaluation of the average size of the crystallites for the
69 oxide samples, but it is less appropriate for reduced samples as the reduction of the cobalt particles is not
70 total and the peaks corresponding of the CoO and Co⁰ phase overlap. In addition, the stacking faults
71 present in the cobalt metallic phase lead to a broadening of the peaks not related with the finite size of the
72 crystallites and requires advanced approaches to take them into account, such as Rietveld analysis or
73 pattern simulation of mixture of cubic and intergrown Co [12]. The dark-field TEM also allows size
74 distribution determination of the crystallites but cannot be easily carried out on used catalysts due to the
75 presence of waxes. Furthermore, both XRD and dark-field TEM give information on the crystallites size,
76 which does not correspond to the nanoparticles size if they are polycrystalline. HAADF-STEM can be
77 used to measure Co nanoparticles, but the contrast between Co and the support is usually too low to be
78 sensitive to the smallest nanoparticles.

79 Given the sensitivity of the X-ray scattering phenomenon to the solely electronic density variations,
80 regardless of the structure or size of the crystal domains considered, small-angle X-ray scattering (SAXS)
81 techniques seem particularly suitable to study the size distributions of metal particles on supports. The
82 first work on the characterization of metallic particles on supported catalysts was carried out in the late
83 1990s by Haubold [13–16] and Benedetti [17,18]. The model systems studied consisted of noble metal
84 particles (Pt or Au) more or less loaded (<1% to 10% by weight of metal) on graphitic matrix. These
85 systems have significant differences in electronic densities between the support and the metal phase and
86 therefore a significant contrast is obtained in anomalous Small angle X-ray scattering (ASAXS). Polizzi
87 et al. [19] have also proposed a detailed critical analysis of the methodologies selected for these studies,
88 insisting on the need for protocols based on numerous controls of the measurement parameters in order to
89 ensure a good control of the uncertainties, which is essential in the case of ASAXS measurements. The
90 ASAXS technique is nowadays seldom used for the characterization of the active phases of catalysts,
91 even if it is well appropriate for a three-phases system (pores, alumina and cobalt nanoparticles).
92 Moreover, scattering techniques have already proved their possibilities to characterize the size and
93 morphology of aggregates [20]. Hence, this technique has the advantage of being able to characterize
94 objects with a size between one nanometer and a few hundred nanometers, thus covering the scales of

95 isolated particles and aggregates of particles. In addition, the analysis can be performed on samples
96 embedded in their waxes, which is very relevant for the case of used FT catalysts.

97
98 In order to study the morphology of the aggregates, advanced techniques such as electron tomography can
99 be successfully applied. Based on TEM technique, electron tomography has been developed during the
100 last decades. The principle is to reconstruct a three-dimensional structure from a series of images (or 2D
101 projections) acquired by rotating the sample in the TEM [21] [22]. In the field of heterogeneous catalysis,
102 it was first used to study the shape and the connectivity of mesoporous networks in catalysts supports
103 such as mesostructured silica [23][24] or zeolites [25][26][27][28]. Individual or supported nanoparticles
104 can also be characterized by electron tomography: in the first case, the morphology (including faceting)
105 of the particles is sought [23], in the latter case, the location inside the support can be explored. As an
106 example, Zecevic et al examined the location of Pt in USY zeolites crystals, showing the presence of Pt
107 particles inside the microporosity [29,29,30]. If the contrast between the nanoparticles and the support is
108 too weak in bright field TEM, chemical sensitive techniques have to be used [21]. EFTEM is mainly
109 employed for characterization of biphasic supports [31] or low Z materials [32]. HAADF-STEM is the
110 preferred technique for supported catalysts [33]. Compared to bright field TEM mode, HAADF-STEM
111 enhances the contrast between the metallic nanoparticles and the oxide support, in as much as the image
112 intensity is proportional to $Z^{1.7}$ [34]. Arslan and al. [35] studied oxide Co aggregates supported on two
113 different alumina supports. They showed a morphology of fully interlocking aggregates/support in the
114 less selective catalyst.

115 Combining SAXS analysis and electron tomography has also been performed by Gommès et al. [36] on
116 Cu catalysts supported on ordered porous silica and allowed illustrating the mesoscale distribution of
117 nanoparticles within supports displaying hierarchical porosity. This study has demonstrated the strong
118 interest of coupling these two kinds of techniques and this approach could be extended to Fischer-Tropsch
119 catalysts provided that SAXS is tuned to ASAXS to specifically focus on cobalt particles and aggregates
120 size.

121
122 The purpose of the present study is to propose a new approach to characterize the cobalt active phase in
123 FT catalysts. We combined two analytical techniques : ASAXS and electron tomography, giving
124 complementary insights on the microstructure and size distribution of both Co nanoparticles and
125 aggregates. A better knowledge of Co aggregates morphology will help to understand their impact on the
126 catalyst performance. This approach, carried out on a Co/alumina-silica catalysts studied first at the oxide

127 state and then at the reduced state, allowed to highlight the mechanisms involved at the nanoscale during
128 the reduction step.

130 **2 Experimental section**

131 **2.1 Catalyst preparation**

132 For this study, we have chosen to focus on two cobalt-based catalysts. They were prepared on a Siralox 5
133 silica-alumina support by incipient wetness impregnation of a nitrate cobalt solution, to obtain an amount
134 of 15 wt.% of cobalt. After impregnation, the catalysts were dried and calcined in air at 400°C. The first
135 sample is the oxide catalyst. The second one is obtained after reduction under pure H₂ flow at 400°C
136 during 16h. After reduction, the reduced catalyst is divided into two fractions: the first fraction is
137 passivated under air in order to be analyzed by electron microscopy and the second fraction is embedded
138 in waxes in order to prevent the re-oxidation and to be analyzed in ASAXS.

140 **2.2 Bulk characterization**

141 XRD measurements were performed on the oxide sample on a PANalytical diffractometer. The most
142 intense Co₃O₄ line (311) was used to calculate the average Co₃O₄ crystallite size with the Scherrer
143 equation. The mean oxide crystallite size was found to be 16.6 ± 2.0 nm.

144 XANES analysis was also carried out on the reduced sample embedded in waxes on the ROCK beamline
145 of SOLEIL synchrotron to determine the reduction rate, which is the ratio between the Co⁰ content (wt
146 .%) and the total Co content. XANES spectrum were decomposed thanks to reference sample spectrum. It
147 has underlined the fact that the reduced sample was partially reduced, with a reduction rate of 47% (see
148 supplementary data, figure 1).

150 **2.3 TEM and HAADF-STEM observations**

151 By bright-field TEM, the contrast between small cobalt nanoparticles and the silica-alumina support is not
152 sufficient to perform precise size measurements. Thus, cobalt particles size was measured by dark field
153 transmission electron microscopy (DF-TEM). Observations were performed using a JEOL 2100F FEG
154 S/TEM, operated at 200 kV. Samples were crushed in ethanol and sonicated. A drop of the suspension
155 was deposited on a Cu grid covered with a holey carbon membrane. DF-TEM observations are performed
156 using the diffraction spots corresponding respectively to the (311), (660) or (220) planes in Co₃O₄ and

157 (100), (002), (101) or (102) planes in hcp Co°. The particles size was measured on a minimum of 200 Co
158 crystallites.

159 Cobalt aggregates were observed and quantified using HAADF-STEM (high angle annular dark field
160 detector in scanning transmission electron microscopy). Before observation, the samples were embedded
161 in an epoxy resin and thin slices (about 70 nm) were cut by ultramicrotomy and transferred onto a Cu grid
162 covered with a holey carbon membrane. Observations were performed using a JEOL 2100F FEG S/TEM,
163 operated at 200 kV. The aggregates size was measured on a minimum of 200 aggregates on several
164 catalysts grains.
165

166 **2.4 Electron tomography**

167 Electron tomography was performed using a JEOL 2100F FEG S/TEM, operated at 200 kV. Samples
168 were prepared as for DF-TEM observations, except that a drop of a gold colloidal suspension was
169 deposited on the grid for further alignment.

170 Images were taken in HAADF-STEM mode, in order to increase the contrast between aggregates and
171 silica-alumina support. Thus, the morphology of the sole aggregate can be visualized without the
172 contribution of the support. Acquisitions were performed using GATAN Digiscan and Digital
173 Micrograph, by rotating the sample inside the microscope over an angular range of $\pm 60^\circ$ using a 1° tilt
174 increment, in equal scheme, which corresponds to 122 pictures for the “oxide sample”, and over an
175 angular range of $+69^\circ$ to -67° using a 2° tilt increment, in Saxton scheme, which corresponds to 93
176 pictures for the “reduced sample”. Dynamic focus adjustment was used for acquisition of the tilt series.

177 Alignment of the HAADF-STEM tilt series was performed thanks to cross-correlation and gold fiducial
178 markers, 3D reconstruction was realized by filtered backprojection (via etomo in IMOD[37,38,38]).

179 Segmentation based on grey-levels histograms was undertaken using AVIZO[®] software. To facilitate
180 segmentation, a pre-processing of the reconstructed volume by a “flowing bilateral filter”[39] was
181 performed. This filter smooths homogeneous regions while preserving the edges of the objects.

182 Morphological geodesic operators were applied in order to extract and quantify the porosity inside the
183 aggregates. Co dispersion in the aggregates was calculated by the ratio between the number of voxels at
184 the surface of the aggregate to the total number of voxels in the aggregate.
185

186 **2.5 ASAXS analysis**

187 2.5.1 Theoretical aspects of ASAXS

188 For the case of spherical particles with a radius R dispersed in a homogeneous matrix, the scattered
 189 intensity is given by:

$$190 \quad I(q) = \frac{N_p}{V_s} (n_p^2 f_p^2 - n_m^2 f_m^2) r_e^2 \int_0^\infty P(R) V(R)^2 F(q, R)^2 \Psi(q) dq \quad (1)$$

191
 192 with N_p the number of particles, V_s the sample volume, n_p and n_m the number density of the atoms in the
 193 particles and in the matrix, f_p and f_m the atomic form factors and r_e the Thomson radius ($r_e = 0.282 \cdot 10^{-12}$
 194 cm).

195 $P(R)$ is the size distribution function, $F(q, R)$ is the form factor and $\Psi(q)$ is the structure factor and
 196 equals to 1 when the particles are well-dispersed.

197
 198 For the case of metal particles supported on a porous matrix, for instance on silica-alumina support, the
 199 simple SAXS analysis (recording at only one energy) is not sufficient to distinguish and to characterize
 200 the nanoparticles as the porous support also contributes significantly to the signal because of the
 201 scattering of the pores.

202 Hence, to isolate the signal specific of each phase, it is therefore interesting to vary the energy of the
 203 incident beam and to perform the measurements near and far the metal (cobalt in our case) absorption
 204 edge.

205 It is recalled that the atomic form factor of a species j can be written:

$$206 \quad f_j(E) = f_0 + f_j'(E) + i f_j''(E) \quad (2)$$

207 with $f_0 = Z$, the atomic number

208 The values of $f_j'(E)$ and $f_j''(E)$ are indicated in the Table 1. We can consider that $f_j''(E)$ does vary
 209 significantly only after the absorption edge.

210

211 **Table 1. Energy-dependent parts of the atomic scattering factor f' and f'' [40,41], near the Co K-**
 212 **edge of absorption (7709 eV).**

	Energy (eV)	f'	f''
E_1	7440	-3.082	0.493
E_2	7648	-4.744	0.470
E_3	7694	-6.356	0.465

213

214

215 Considering a system of particles p supported on a porous support s and with air filling the pores, the
 216 scattered intensity can be written thanks to the partial structure factors S_{pp} , S_{ss} and S_{sp} described by
 217 Binninger et al. [42] as followed :

$$218 \quad \langle I(q, E) \rangle = |f_p(E)|^2 n_p^2 r_e^2 S_{pp}(q) + |f_s|^2 n_s^2 r_e^2 S_{ss}(q) + 2\Re(f_p(E)f_s^*) n_p n_{ps} r_e^2 S_{sp}(q) \quad (3)$$

219 The difference between the intensities measured at two different energies E_1 et E_2 leads to :

220

$$\begin{aligned} \langle I(q, E_1) \rangle - \langle I(q, E_2) \rangle &= n_p^2 r_e^2 \left(|f_p(E_1)|^2 - |f_p(E_2)|^2 \right) S_{pp}(q) + 2f_s \left(f_p(E_1) - f_p(E_2) \right) n_p n_s r_e^2 S_{sp}(q) \\ &= 2n_p r_e^2 \left(f_p(E_1) - f_p(E_2) \right) \cdot \left(n_p \bar{f}_p S_{pp}(q) + n_s f_s S_{sp}(q) \right) \\ &= 2n_p^2 r_e^2 \bar{f}_p \left(f_p(E_1) - f_p(E_2) \right) \cdot (S_{pp} + \alpha S_{sp}) \end{aligned} \quad (4)$$

221

222

223 where $\bar{f}_p = \frac{f_p(E_1) + f_p(E_2)}{2}$ is the mean value of $f_p(E)$ and $\alpha = \frac{n_s f_s}{n_p \bar{f}_p}$

$$224 \quad S_{pp}(q) = \frac{N_p}{V_s} \int_0^{+\infty} P_p(R_p) V(R_p)^2 F(q, R_p)^2 dR_p \quad (5)$$

$$225 \quad S_{mp} = \frac{N_p}{V_s} \iint_0^\infty P_p(R_p) P_s(R_s) V(R_p) V(R_s) F(q, R_p) F(q, R_s) \frac{\sin(q(R_p+R_s))}{q(R_p+R_s)} dR_p dR_s \quad (6)$$

226 As a first approach, we can consider that the term αS_{sp} is negligible before S_{pp} if $\alpha < \frac{\langle V(R_p)^2 \rangle}{\langle V(R_p) \rangle \langle V(R_s) \rangle}$.

227 In our case:

- 228 - we have calculated for E_1 and E_2 energies, an α close to 0.55
- 229 - the size of the pores and of the particles are in the same order of magnitude, so that $\frac{\langle V(R_p)^2 \rangle}{\langle V(R_p) \rangle \langle V(R_s) \rangle}$ is
 230 higher than 1.

231 It can be concluded that in the present case of the cobalt-based catalysts, the contribution of the support-
 232 particle interaction term is negligible. Indeed, as explained by Morfin et al [10], the particles are big
 233 enough and their volume fraction is small compared to the aluminum support consequently the
 234 probability of interference between the cobalt particles and the support is low.

235 It follows :

$$236 \quad \langle I(q, E_1) \rangle - \langle I(q, E_2) \rangle \approx 2n_p^2 r_e^2 \bar{f}_p \left(f_p(E_1) - f_p(E_2) \right) \cdot S_{pp}(q) \quad (7)$$

$$237 \quad \langle I(q, E_1) \rangle - \langle I(q, E_2) \rangle \approx \frac{N_p}{V_s} n_p^2 r_e^2 \left(|f_p(E_1)|^2 - |f_p(E_2)|^2 \right) \int_0^{+\infty} P_p(R_p) V(R_p)^2 F(q, R_p)^2 dR_p \quad (8)$$

238

239 Finally, when the porosity is filled with waxes, the difference in electron density between particles and
 240 waxes should be taken as contrast factor instead of the electron density of the particle itself. Therefore the
 241 previous expression becomes :

$$242 \langle I(q, E_1) \rangle - \langle I(q, E_2) \rangle \approx$$

$$243 \frac{N_p}{V_s} r_e^2 \left(|n_p f_p(E_1) - n_m f_m(E_1)|^2 - |n_p f_p(E_2) - n_m f_m(E_2)|^2 \right) \int_0^{+\infty} P_p(R_p) V(R_p)^2 F(q, R_p)^2 dR_p \quad (9)$$

244

245 2.5.2 ASAXS measurements

246 For ASAXS analysis, the reduced sample was directly embedded in waxes without air exposition in order
 247 to prevent reoxidation. The oxide sample was also put into waxes in order to keep the same mode of
 248 sample preparation. Then, pellets with a thickness of approximately 300 μ m were prepared. Anomalous
 249 small-angle X-ray scattering experiments have been performed on the SWING beamline at synchrotron
 250 SOLEIL. It involves characterizing cobalt nanoparticles supported on a porous silica-alumina by
 251 recording SAXS images around its absorption edge. The advantage of performing ASAXS analyzes is
 252 that it suppresses the contribution of the porous support. For this purpose, it is necessary to be close to the
 253 cobalt absorption threshold in order to vary the diffusion factor of Co and thus of the particles, but also to
 254 keep constant the diffusion factor of the support. Hence, the scattered intensity was measured at three
 255 different energies (see Table 1) 7440, 7647 and 7694eV, slightly below the cobalt K-edge of absorption.
 256 The incident beam energy has been calibrated with a metallic cobalt foil. To cover the largest q range,
 257 two sample-detector distances (1000 mm and 6000 mm) have been selected. Furthermore, to increase the
 258 sensibility of the photons counting on the peripheral part of the detector, two kinds of beamstop (a small
 259 beamstop with a size of 2x1 mm² and larger beamstop with a size of 3x3 cm²) were used. Using the large
 260 beamstop, allowed to recorded 2D images with longer exposure time, by masking the strong diffusion
 261 around the small beamstop, in order to get better statistics for high q values. In total, four different
 262 configurations (detector-sample distance, beamstops) have been used.

263 The scattering images were recorded using a AVIEX PCCD170170 detector. To increase the statistic of
 264 the scattering intensity, thirty images were acquired for each energy and at each detector-sample
 265 configuration. The acquisition time was function of the configuration and was chosen in order not to
 266 saturate the detector.

267 Through 1D reduction, raw data were corrected with respect to: acquisition time, geometrical effects like
 268 the projection of the detector plane on the sphere with radius equal to the sample-detector distance,
 269 detector sensitivity (3ADU/ph, Noise \approx 2ADU), the incoming-photon flux and finally averaged to increase the
 270 statistic. The scattering background coming from all components in the beamline and from the air was

271 measured before each series of acquisition, for each energy and at each configuration. The sample
272 transmission was calculating thanks to the measurement of the incoming and transmitted intensities. It
273 allowed correction of the intensity from the real thickness (e) of the sample, calculated thanks to the
274 composition of the sample obtained by X-Ray Fluorescence and with the following equation:

$$e = -\frac{\ln T}{\mu_{\text{sample}}} \quad (10)$$

275
276
277
278 T being the transmission and μ_{sample} the linear absorption coefficient (cm^{-1}).

279
280 In order to calibrate the intensity in absolute unities, i.e expressed as differential scattering cross section
281 per unit volume in cm^{-1} , a calibrated NIST glassy carbon [43], was measured at each energy and each
282 configuration. A correction factor has been calculated from the ratio between the NIST data and the
283 experimental data.

284 2.5.3 Modelling of ASAXS data

285 The ASAXS results for both oxide and reduced catalysts are given in Figure 1. The plotted curves were
286 obtained from the subtraction of the intensity measured at $E_2 = 7647$ eV and the intensity measured at E_3
287 $= 7694$ eV near the cobalt K-edge of absorption. Noticeable differences can be observed in the q-range
288 between $2.3 \cdot 10^{-2} \text{ \AA}^{-1}$ and $1.2 \cdot 10^{-3} \text{ \AA}^{-1}$.

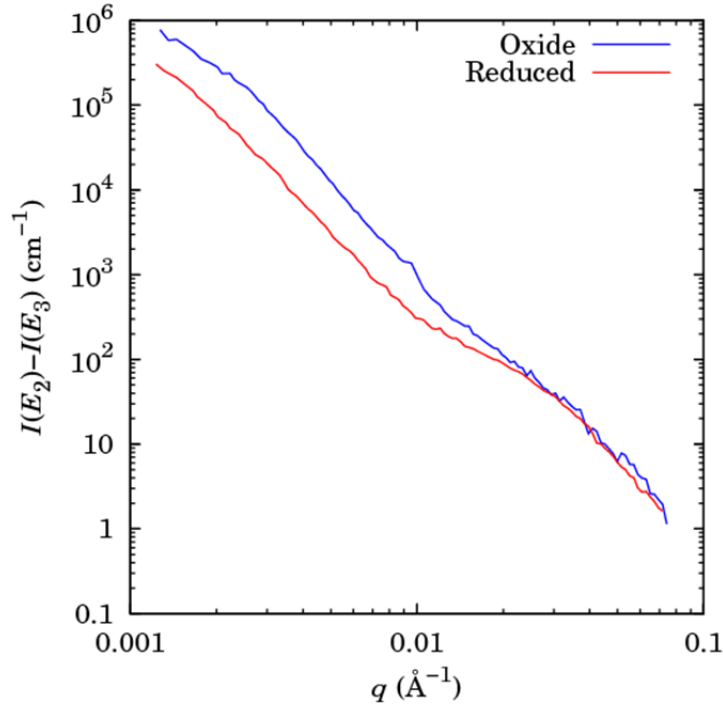


Figure 1. ASAXS curves obtained on oxide and reduced samples

In order to evaluate the size distribution of the cobalt particles, a nonlinear least squares adjustment of the ASAXS signal is performed. The assumptions made for the choice of the regression model are listed below.

Given the shape of the curves (two inflections of the scattered signal), the experimental data could not be fitted with only one function of size distribution. It appears that two kinds of cobalt particles exist in the catalyst, at the oxide and at the reduced state, at two different scales. Based on the electron microscopy observations, these two populations are attributed to isolated, dense and crystalline particles at the small scale, and to larger, polycrystalline and moderately dense aggregates at large scale. This assumption will be corroborated in this paper.

For the cobalt phase, we thus consider that the scattering objects can be porous. The porosity is so called ε and is filled with waxes. In the case of the crystalline particles, $\varepsilon = 0$ and in the case of cobalt aggregate, $\varepsilon > 0$.

The number of cobalt atoms in the scattering object and the number of the matrix atoms are respectively defined by:

$$N_{Cox} = \frac{N_A \times \rho_{Cox}}{M_{Cox}} \times V \times (1 - \varepsilon) \quad (11)$$

$$N_m = \frac{N_A \times \rho_m}{M_m} \times V \times \varepsilon \quad (12)$$

With $\text{Co}_x = \text{Co}_3\text{O}_4$ in the case of oxide cobalt and $\text{Co}_x = \text{Co}^0$ in the case of metallic cobalt, V the volume of the scattering object, N_A the Avogadro number ($6.022 \times 10^{23} \text{ mol}^{-1}$), M_{Co_x} and M_m the molar masses in g/mol, ρ_{Co_x} and ρ_m the densities of both phases in g/cm^3 .

Hence, the scattering factor of a cobalt particle is defined by :

$$n_p f_p = \left(\frac{N_A \times \rho_{\text{Co}_x}}{M_{\text{Co}_x}} \times f_{\text{Co}_x} \right) \times (1 - \varepsilon) + \left(\frac{N_A \times \rho_m}{M_m} \times f_m \right) \times \varepsilon \quad (13)$$

It follows:

$$n_p f_p - n_m f_m = \left(\frac{N_A \times \rho_{\text{Co}_x}}{M_{\text{Co}_x}} \times f_{\text{Co}_x} - \frac{N_A \times \rho_m}{M_m} \times f_m \right) \times (1 - \varepsilon) = (n_{\text{Co}_x} f_{\text{Co}_x} - n_m f_m) \times (1 - \varepsilon) \quad (14)$$

The term $\frac{N_p}{V_s}$ of the equation (9) can be expressed as:

$$\frac{N_p}{V_s} = \frac{w_{\text{Co}_x} \times \rho_s}{\rho_{\text{Co}_x}} \times \frac{1}{1 - \varepsilon} \times \frac{1}{\langle V \rangle} \quad (15)$$

With $\langle V \rangle$ the mean volume of the particle aggregate (cm^{-3}), w_{Co_x} the weight content of the cobalt phase (wt.%), ρ_s the sample density in g/cm^3 .

The particles are considered to be spherical and isolated: as so, the structure factor is not taken into account while the form factor is. Thus the form factor for a spherical particle is:

$$F^2(q, R_p) = \left[3 \frac{\sin(q, R_p) - q R_p \cos(q, R_p)}{(q, R_p)^3} \right]^2 \quad (16)$$

$$\text{and } V(R_p) = \frac{4}{3} \pi R_p^3 \quad (17)$$

The size distributions can be represented by a sum of log-normal distribution:

$$P_i(R_p) = \frac{1}{\sqrt{2\pi} R_p \sigma_i} \exp\left(-\frac{(\ln R_p - \mu_i)^2}{2\sigma_i^2}\right) \quad (18)$$

In order to calculate the number and volume average sizes from the adjusted log-normal distribution, the distribution moments M_n must be known [44]:

$$M_n = \exp\left(\mu n + \frac{n^2 \sigma^2}{2}\right) \quad (19)$$

The volume size distribution P_v is defined by:

$$P_{iv}(R_p) = \frac{R_p^3 P(R_p)}{M_3} \quad (20)$$

The number, the surface and the volume mean sizes can be calculated:

$$R = \frac{M_1}{M_0} = \exp\left(\mu + \frac{\sigma^2}{2}\right), R_{surf} = \frac{M_3}{M_2} = \exp\left(\mu + \frac{5\sigma^2}{2}\right) \text{ and } R_{vol} = \frac{M_4}{M_3} = \exp\left(\mu + \frac{7\sigma^2}{2}\right) \quad (21)$$

Given the shape of the curves (two inflections of the scattered signal), we chose to model the distribution of cobalt by two log-normal distributions:

$$\begin{aligned} \langle I(q, E_1) \rangle - \langle I(q, E_2) \rangle & \approx r_e^2 \left(|n_p f_p(E_1) - n_m f_m(E_1)|^2 - |n_p f_p(E_2) - n_m f_m(E_2)|^2 \right) \\ & \times \left[\frac{N_{p1}}{V_s} \int_0^{+\infty} P_1(R_p) V(R_p)^2 F(q, R_p)^2 dR_p + \frac{N_{p2}}{V_s} \int_0^{+\infty} P_2(R_p) V(R_p)^2 F(q, R_p)^2 dR_p \right] \end{aligned} \quad (22)$$

With

$$\frac{N_{p1}}{V_s} = \frac{w_{Cox} \times \rho_s}{\rho_{Cox}} \times w_1 \times \frac{1}{1-\varepsilon_1} \times \frac{1}{\langle V_1 \rangle} \text{ and } \frac{N_{p2}}{V_s} = \frac{w_{Cox} \times \rho_s}{\rho_{Cox}} \times w_2 \times \frac{1}{1-\varepsilon_2} \times \frac{1}{\langle V_2 \rangle} \quad (23)$$

$\langle V \rangle$ is the mean volume such as :

$$\langle V \rangle = \frac{4}{3} \times \pi \times \int R_p^3 P(R) dR = \frac{4}{3} \times \pi \times M_3 = \frac{4}{3} \times \pi \times \exp\left(3\mu + \frac{9\sigma^2}{2}\right) \quad (24)$$

Supposing that the first particle population corresponds to dense, crystalline and isolated particles and that the second one is attributed to aggregates partially dense, the previous equation becomes:

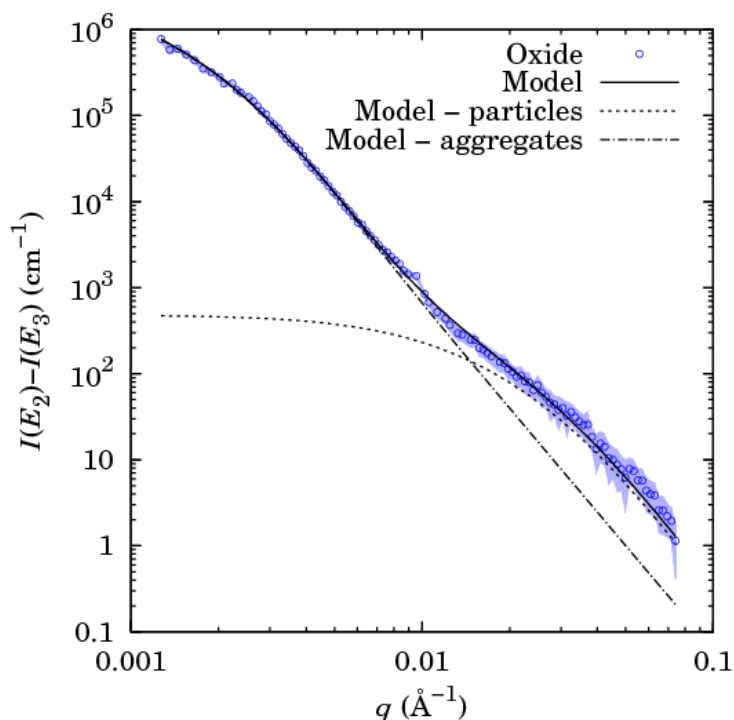
$$\begin{aligned} \langle I(q, E_i) \rangle - \langle I(q, E_j) \rangle & = w_{Cox} \times w_1 \times \frac{\rho_s}{\rho_{Cox}} \times \Delta \rho_{Cox}^2(E_i, E_j) \\ & \times \left[\frac{1}{\langle V_1 \rangle} \int_0^{+\infty} P_1(R_p) V^2(R_p) F^2(q, R_p) dR_p + \frac{w_2(1-\varepsilon_2)}{w_1} \times \frac{1}{\langle V_2 \rangle} \int_0^{+\infty} P_2(R_p) V^2(R_p) F^2(q, R_p) dR_p \right] \end{aligned} \quad (25)$$

With w_1 and w_2 the cobalt weight percent of the first and second population of particles, and

$$\Delta \rho_{Cox}^2(E_i, E_j) = (n_{Cox} f_{Cox}(E_i) - n_m f_m)^2 \times r_e^2 - (n_{Cox} f_{Cox}(E_j) - n_m f_m)^2 \times r_e^2 \quad (26)$$

This model allows estimating the size distribution of the particles (μ_1, σ_1), the size distribution of the aggregates (μ_2, σ_2) and the parameter $\frac{w_2(1-\varepsilon_2)}{w_1}$ which depends on the ratio between the cobalt content included in the first and in the second population, but also on the porosity of the aggregates.

360 An example of fit is shown on Figure 2 for the oxide sample. The first part of the curve (from 10^{-1} \AA^{-1} to
361 $1.4 \cdot 10^{-2} \text{ \AA}^{-1}$) is essentially due to the contribution of the first population of small-size particles whereas
362 the second part of the curve (from $1.4 \cdot 10^{-2} \text{ \AA}^{-1}$ to $1.2 \cdot 10^{-3} \text{ \AA}^{-1}$) is due to the contribution of the second
363 population of larger objects called aggregates.
364



365

366 **Figure 2. Fit of the experimental ASAXS data of the oxide sample.**
367

368 **3 Results**

369 **3.1 Particle scale**

370 Cobalt particle size distribution was measured by dark-field transmission electron microscopy and also
371 obtained by ASAXS.

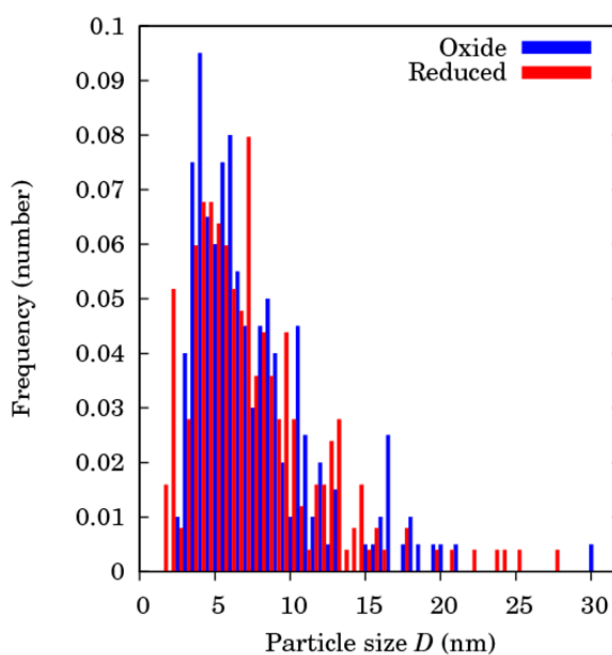
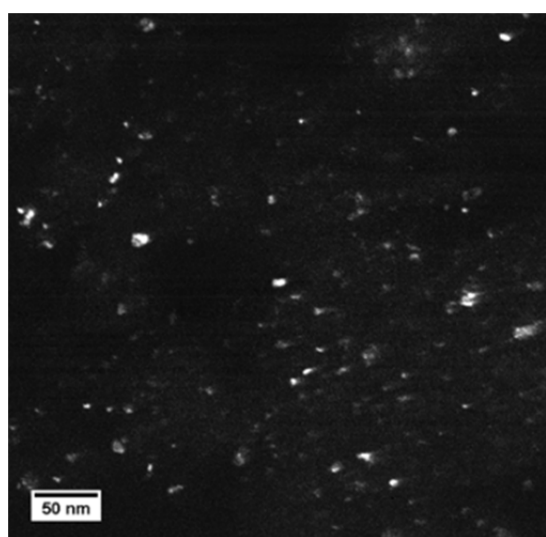
372 Figure 3a presents a representative image of dark-field TEM of cobalt nanoparticles supported on silica-
373 alumina. Figure 3b presents the size distribution in both oxide (blue) and reduced (green) catalysts. Both
374 size distributions present the same general shape, and few differences are observed.

375 Besides, the volume size distribution (P_v) of the particles obtained by ASAXS for both catalysts thanks to
376 the fit of the experimental data are plotted on Figure 4. The two size distributions are slightly different as

377 revealed by the μ and σ parameters of the lognormal-law (3.29 and 0.56 for the oxide sample versus 3.56
378 and 0.44 for the reduced sample) however the differences are faint.

379
380 In order to compare TEM, ASAXS measurements and XRD mean size, all results are expressed by the
381 volume mean particle radius. ASAXS, TEM and XRD data on oxide samples are totally consistent,
382 considering uncertainties of both techniques. It is noteworthy that a very good agreement is obtained
383 between ASAXS and TEM results for the oxide sample contrary to the case of the reduced sample. This
384 can be accounted for by the 47% reduction rate, measured by XANES. Indeed, less than half of the cobalt
385 is reduced and thus in the metallic Co^0 phase. Moreover, it is known that the small particles are less
386 reducible than the big ones. Due to its principle, the dark-field TEM allows observing and counting solely
387 Co^0 particles, whereas the ASAXS technique characterizes all the cobalt either oxide or metallic. This
388 could explain the mean size differences obtained with both techniques, and also the higher mean size
389 particle measured on the reduced sample by TEM compared to the oxide catalyst.

390 These ASAXS analyses tend to show a decrease in size during reduction, which agrees with the fact that
391 the reduced Co^0 particles are smaller than the oxide Co_3O_4 particles due to the crystallographic structure
392 contraction of around 0.8. However it is difficult to conclude on the effect of the reduction of the particle
393 size as it seems to be very tight and hidden by the large distribution of the particle size and the significant
394 heterogeneity of the samples.

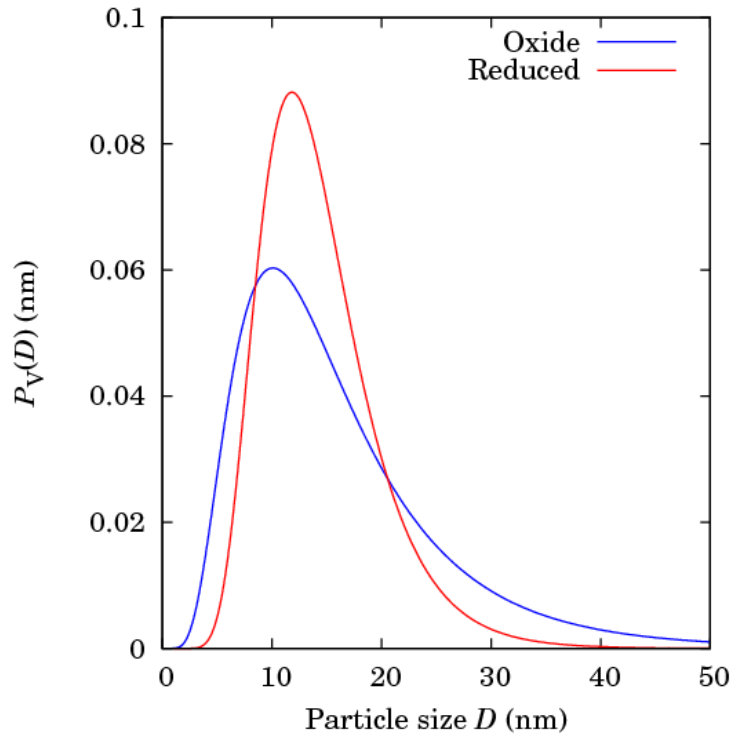


396
397 **Figure 3 : a) Dark-field TEM image of oxide Co/silica-alumina. B) Particles size distribution**
398 **expressed by number frequency: in oxide catalyst (blue) and reduced catalyst (red)**

399
400
401
402
403
404

Table 2: Cobalt particle sizes measured by different techniques

	Oxide catalyst	Reduced catalyst
DF TEM – volume mean size (nm)	16.1 ± 2.4	18.0 ± 2.7
ASAXS - volume mean size (nm)	16.2	14.5
XRD – volume mean size (nm)	16.6 ± 2.0	/



405
406
407
408

Figure 4 : Volume size distribution (P_V) obtained for the oxide and the reduced catalysts by ASAXS.

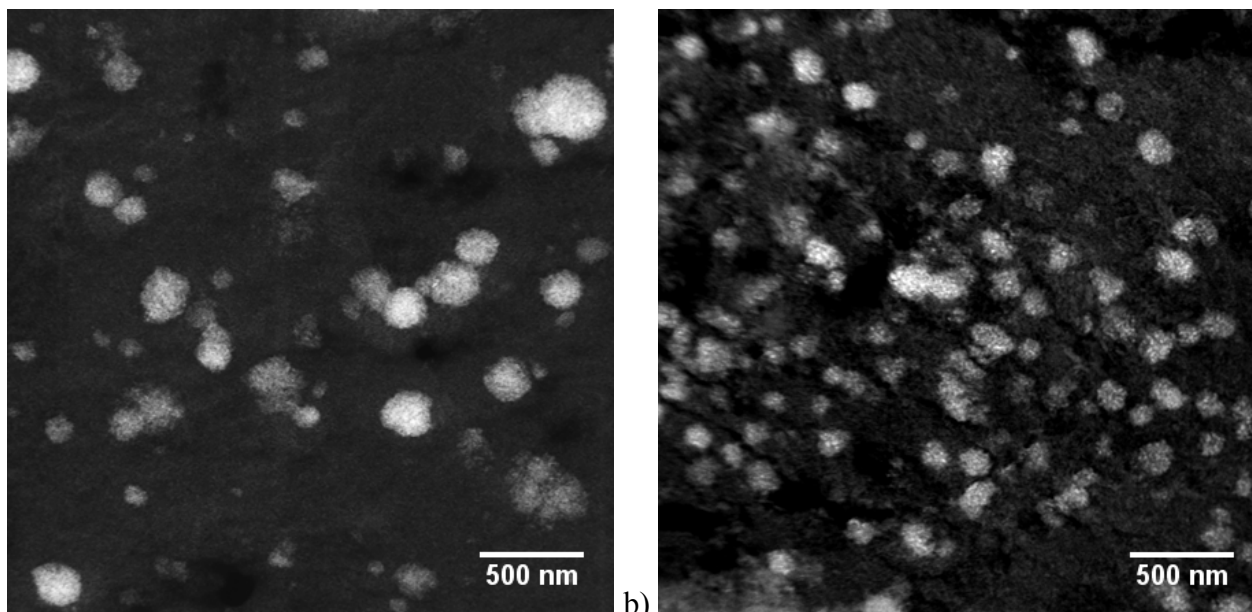
3.2 Cobalt aggregates characterization by HAADF-STEM and electron tomography

Cobalt aggregates in the catalysts grains were observed at different scales. First of all, SEM observations on several grains of the oxide catalyst were performed and have showed a strong heterogeneity in the Co aggregates repartition inside a grain and from on grain to another. Furthermore, the scale of characterization was too large to precisely their size. Thus, HAADF-STEM observations were carried out on ultramicrotomy cuts. Representative images for the oxide and reduced catalysts are presented on

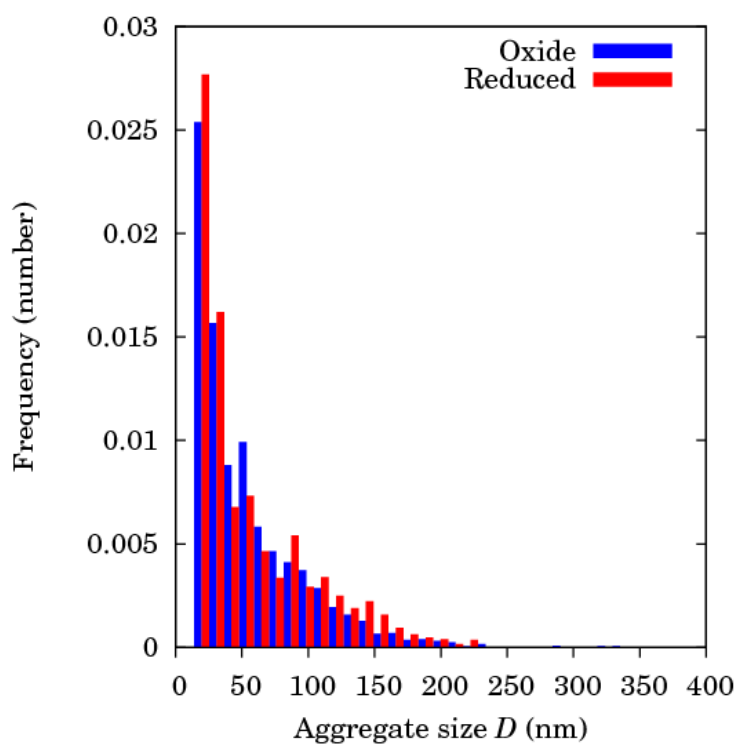
415 Figure 5. They have revealed that aggregates repartition and even size can strongly vary from a grain to
416 another. Nevertheless, measurements were performed on more than 200 aggregates in each catalyst and
417 their size distribution is presented on Figure 6. The mean size in oxide catalyst corresponds to 52 nm and
418 to 54 nm in reduced one.

419 ASAXS analysis has also allowed to obtain the number size distribution (P_N) of the aggregates for both
420 catalysts thanks to the fit of the experimental data (see Figure 7). The maximum of the distribution in the
421 reduced sample is slightly shifted to smaller size than in the oxide one. The mean number size of the
422 oxide catalyst is 85 nm versus 49 nm for the reduced one. However the standard deviation is quite high,
423 meaning that the aggregates size can vary from 20 to almost 200 nm. : the lognormal-law parameters (μ
424 and σ that are, respectively) were found to be 5.91 and 0.55 for the oxide catalyst and 5.16 and 0.83 for
425 the reduced one.

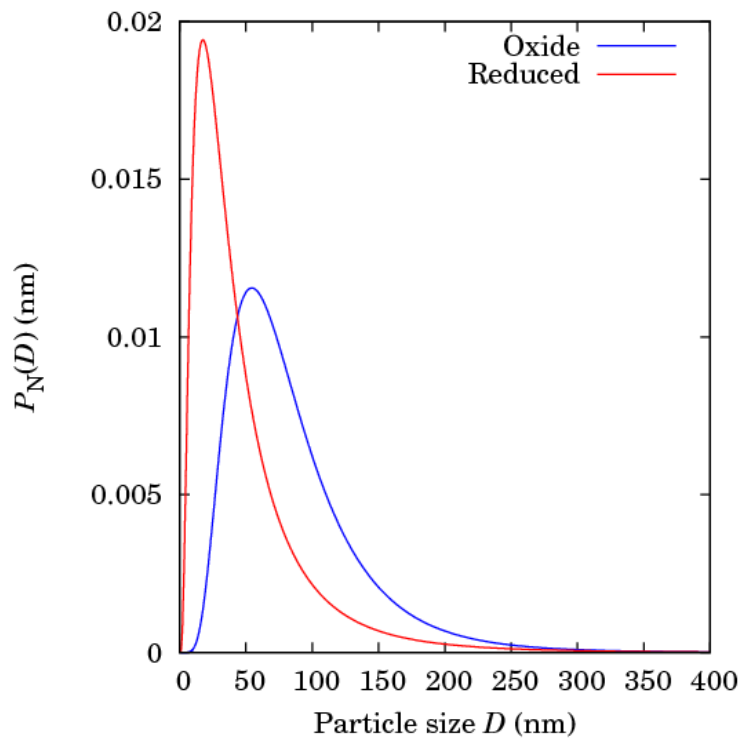
426 ASAXS and STEM measurements are in good agreement concerning the aggregates mean size of the
427 reduced sample (54 and 49 nm) but a small difference exists for the oxide sample, even if the ASAXS and
428 STEM values (52 and 85 nm) are in the same order of magnitude. However, we have discussed that the
429 sample heterogeneity and the cobalt distribution from one grain to another was significant, which could
430 explain the differences. Considering heterogeneity of the samples and standard deviations of the
431 distribution, it can be concluded that the aggregate diameter does not evolve significantly during
432 reduction. Hence, reduction under H_2 at $400^\circ C$ does not lead to aggregate sintering neither to large scale
433 redistribution of cobalt in the support. Cobalt aggregates microstructure was studied by dark-field
434 transmission electron microscopy. Both electron diffraction patterns and DF-TEM images reveal an
435 important change of morphology during reduction. Indeed, oxide cobalt aggregates present a dense
436 structure with indistinct particles, i.e consisting of coherent domains having rather the same crystalline
437 orientation but with some structural stacking faults (Figure 9). On the other hand, metallic cobalt
438 aggregates present a clearly polycrystalline structure (Figure 10), and crystals forming the aggregates
439 even seem to be disjoint. It is confirmed by high magnification HAADF-STEM images (Figure 8). In
440 oxide catalyst, aggregates look compact, with a uniform contrast, whereas in reduced catalyst, individual
441 particles forming the aggregates on metallic form appear clearly and some porosity is visible in between.
442



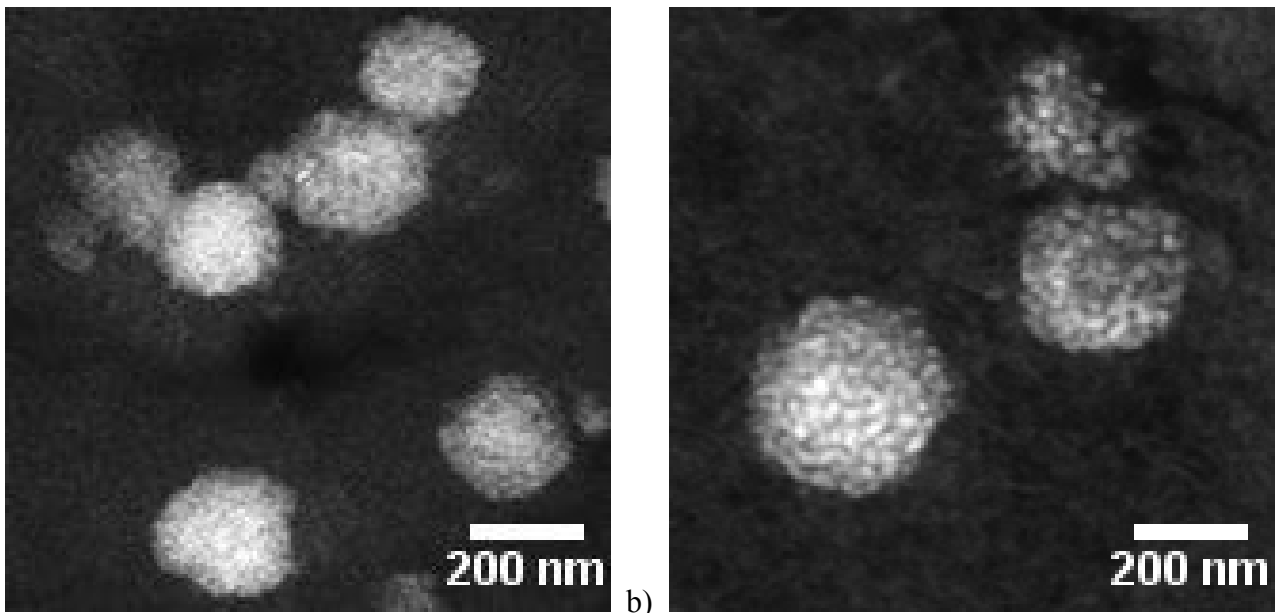
443 a) b)
 444 **Figure 5 : HAADF-STEM images of a) oxide catalyst ; b) reduced catalyst.**
 445



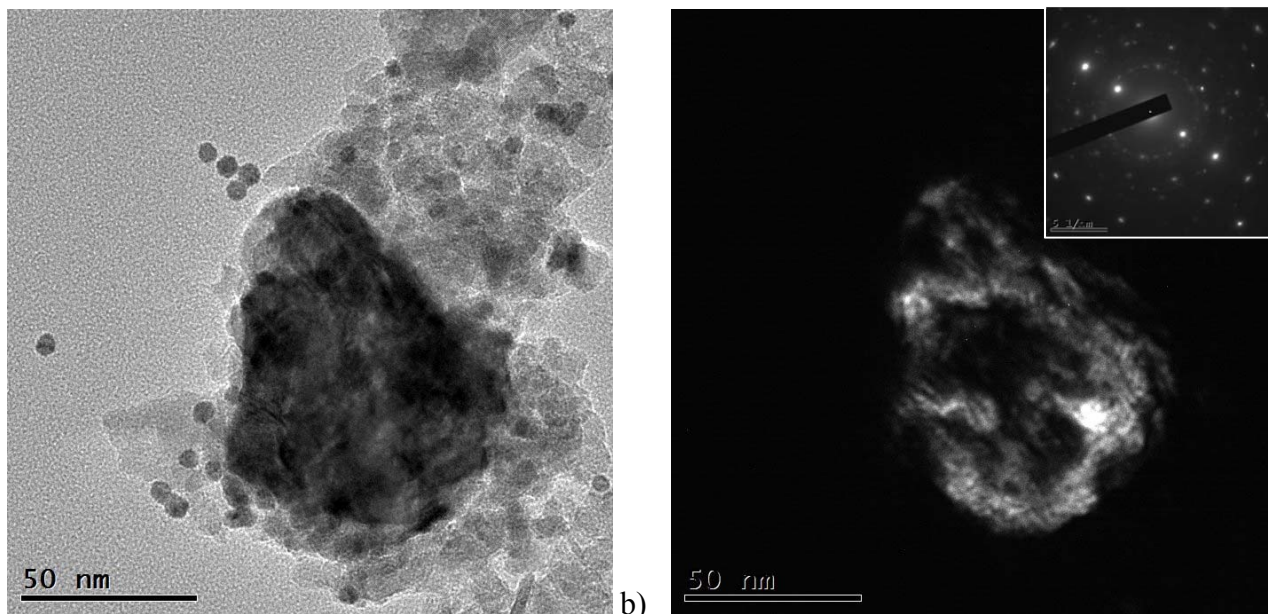
446
 447 **Figure 6 : Cobalt aggregates size distribution, measured by HAADF-STEM, expressed by number**
 448 **frequency: in oxide catalyst (blue) and reduced catalyst (red)**
 449



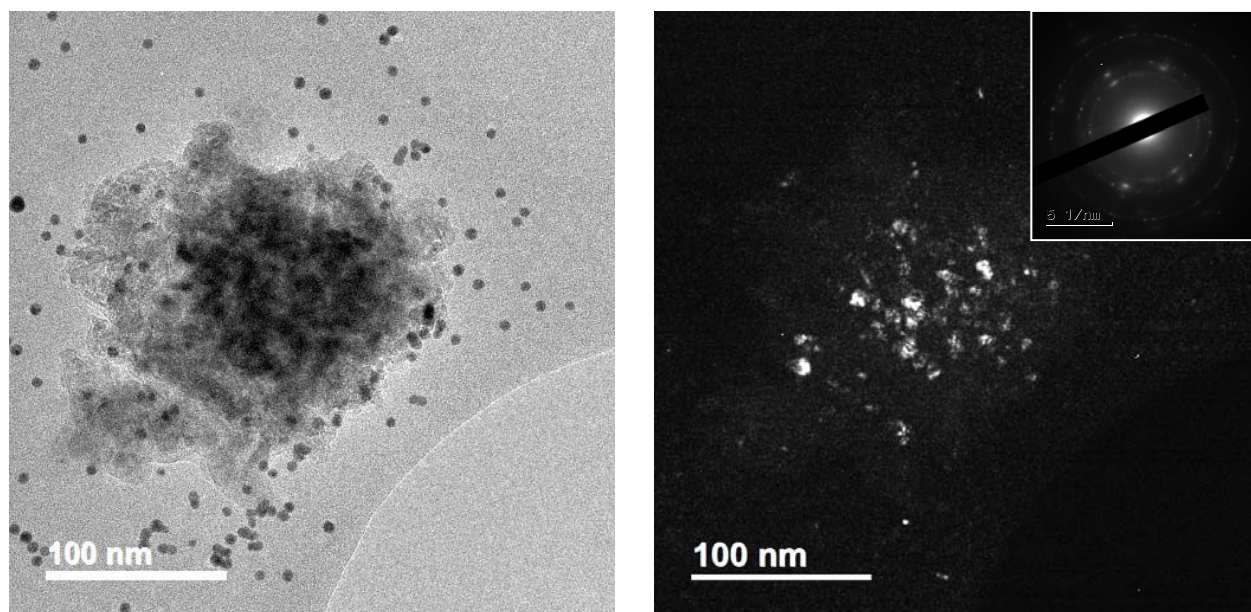
450
451 **Figure 7 : Number aggregates size distribution (P_N) obtained by ASAXS for the oxide and the**
452 **reduced catalysts.**
453



454 a) b)
455 **Figure 8 : High magnification HAADF-STEM images of a) oxide catalyst ; b) reduced catalyst.**
456



457 a) b)
 458 **Figure 9 : a) Bright-field TEM ; b) Dark field TEM images and in insert electron diffraction**
 459 **pattern of a cobalt aggregate in the oxide catalyst.**
 460



461
 462 **Figure 10 : a) Bright-field TEM ; b) Dark field TEM images and in insert electron diffraction**
 463 **pattern of a cobalt aggregate in the reduced catalyst.**
 464

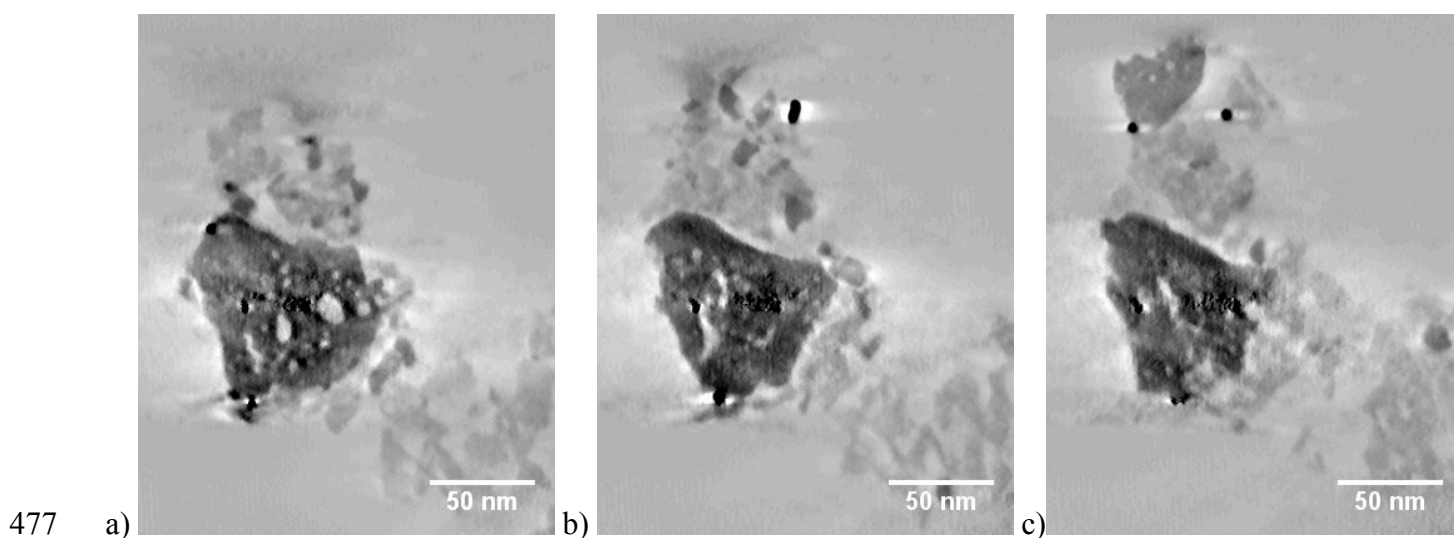
465 Combination of several TEM imaging modes gives an insight of a strong modification of the aggregates
 466 morphology during reduction. Nevertheless, these are 2D techniques and they are not able to fully
 467 describe their morphology. Three-dimensional morphology can be described by electron tomography.

468 Two different aggregates for each sample were studied by electron tomography. They were chosen
 469 according to their size. Too small aggregates (circa 20 nm) may be mistaken to large particles, too large

470 aggregates (> 100 nm) are too thick for electron tomography acquisitions. 50 nm-diameter aggregates
471 were selected, corresponding to the mean size obtained from HAADF-STEM images.

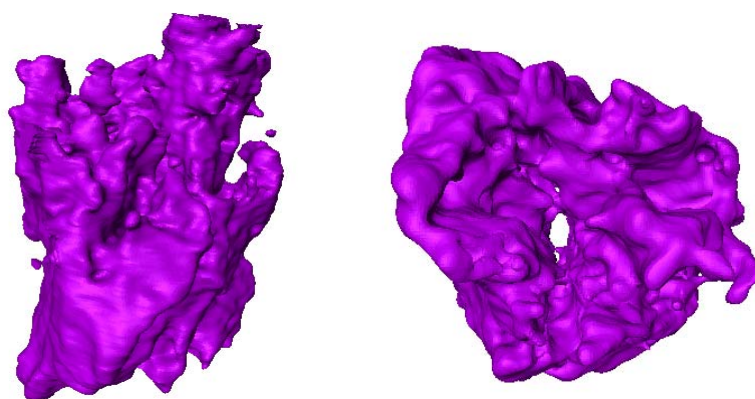
472 Figure 11 depicts cross sections of the reconstructed volume of a cobalt aggregate in the oxide catalyst.
473 The aggregate appears in dark in the image (the contrast was inverted after the acquisition and before
474 reconstruction) and the support is visible in light grey. The aggregate is a compact and dense phase of
475 cobalt, with some spherical or cylindrical closed pores in its centre.

476



478 **Figure 11 : a-c) Slices from electron tomography reconstructions for a cobalt aggregate in the oxide**
479 **catalyst.**

480



481

482 **Figure 12: Model of a cobalt aggregate in the oxide catalyst, obtained by segmentation of the**
483 **electron tomography reconstruction. Two different orientations.**

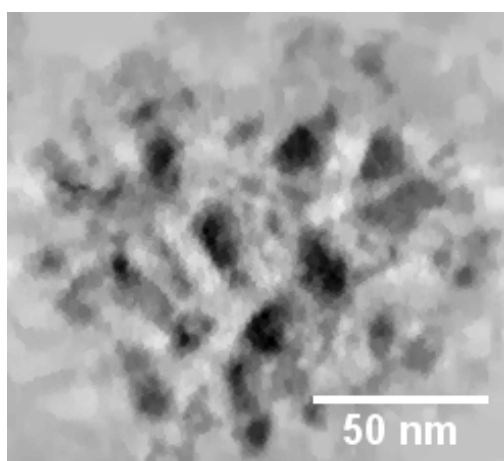
484

485 Segmentation of the reconstructed volume allowed to model the aggregate. A 3D representation of the
486 model aggregate is presented on Figure 12. Only the cobalt phase was segmented independently to the

487 silica-alumina support. Indeed, the contrast of the support compared to porosity is too weak to be
488 segmented without important error. It confirms the compact structure of the aggregate. In particular, the
489 external surface of the aggregate is very smooth. Accessibility of cobalt is a key factor for catalysis. We
490 defined two parameters to estimate the accessibility of cobalt in aggregates. The first one, called
491 “aggregate dispersion”, is calculated as the ratio between surface cobalt to total cobalt and the second one
492 is the porosity inside the aggregate. From the aggregate model obtained by electron tomography, the
493 “aggregate dispersion” is estimated to 18% and the porosity to 35%. “Aggregate dispersion” takes into
494 account the surface roughness of the aggregate and is different from dispersion classically obtained by
495 chemisorption.

496 Figure 13 depicts a cross section of the reconstructed volume of a cobalt aggregate in the reduced
497 catalyst. The aggregate appears in dark in the image. Here, the support is slightly visible compared to
498 porosity. The aggregate is a porous and airy phase of cobalt, composed of almost independent particles
499 with large inter-particle porosity.

500 A 3D representation of the model aggregate, obtained by segmentation of the reconstructed volume is
501 presented on Figure 14. Here again, only the cobalt phase was selected for modeling independently from
502 the support. The sponge-like structure of the cobalt aggregate in the reduced sample is clearly highlighted.
503 Contrary to the compact morphology on the oxide state, the aggregate presents a large external surface,
504 leading to high accessibility. From the aggregate model, the “aggregate dispersion” is estimated to 27%
505 and the porosity to 65%.



507
508 **Figure 13 : Slice from electron tomography reconstructions for a cobalt aggregate in the reduced**
509 **catalyst.**
510

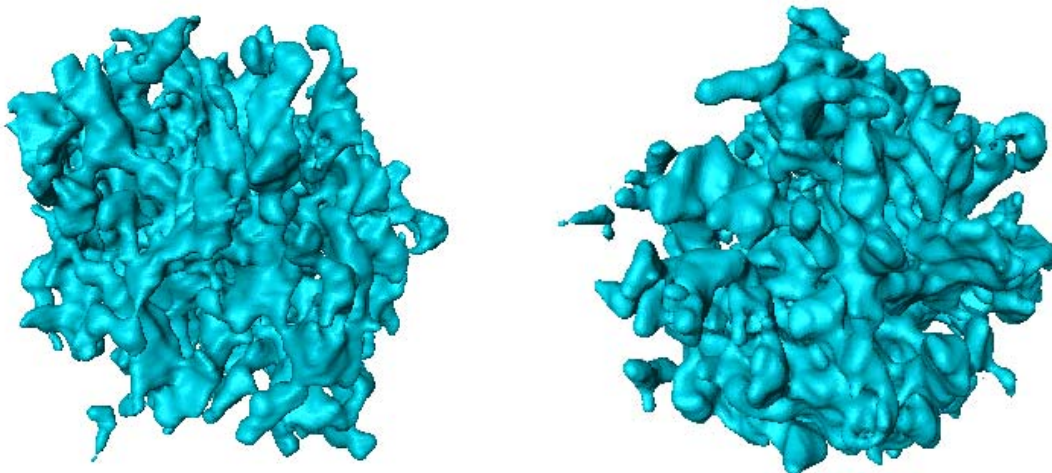


Figure 14: Model of a cobalt aggregate in the reduced catalyst, obtained by segmentation of the electron tomography reconstruction. Two different orientations.

Besides these deep electron tomography characterizations, ASAXS also provides information on the aggregate structure. Indeed, the model used to fit the ASAXS data makes it possible to calculate the $\frac{w_2(1-\varepsilon_2)}{w_1}$ parameter. It was found to be 3.05 for the oxide sample and 1.11 for the reduced sample.

Supposing that the ratio between the cobalt content included in the first and in the second populations (particles and aggregates) does not evolve during the reduction step, we can suggest that the ratio $\frac{(1-\varepsilon_2)_{reduced}}{(1-\varepsilon_2)_{oxide}}$ equals to 0.364, which implies that the compacity of the reduced aggregates ε_2 is almost 2.8 times less significant than the one of the oxide aggregates. Hence, ASAXS analysis also lead to conclude that during the reduction, the aggregate structure becomes airier and more porous.

Furthermore, to check the good agreement between ASAXS and electron tomography, setting the oxide aggregate porosity equal to 35% as calculated by electron tomography, the ratio $\frac{(1-\varepsilon_2)_{reduced}}{(1-\varepsilon_2)_{oxide}}$ of 0.364 obtained by ASAXS leads to a calculated aggregate porosity of 76% for the reduced sample. Even if the porosity is not exactly the same when calculated by electron tomography or by ASAXS, the same trend is observed with the same order of magnitude. Both techniques are in good agreement but each provides different benefits. Electron tomography provides local information and could suffer from representativeness issues, it allows visualizing the object of the study and justify the kind of model employed to fit the ASAXS data (spherical particles and aggregates, log-normal distribution of size). Besides, ASAXS technique is less familiar but as the advantage to be a bulk analysis which provides representative information of the whole sample. Hence, both technique are complementary.

533 They underline the strong effect of the reduction step on the aggregate structure: the oxide aggregate are
534 dense with indistinct particles, i.e consisting of coherent domains having rather the same crystalline
535 orientation, but structural stacking faults and with some spherical or cylindrical closed pores, whereas the
536 reduced aggregates are clearly polycrystalline with visible individual particles with large inter-particle
537 porosity, which leads to a porous and airy structure. The oxide aggregate porosity is certainly formed
538 during the calcination step under thermal stresses or due to defects relative to the non-uniform cobalt
539 impregnation. The reduced aggregate porosity is formed during the reduction step and is supposed to be
540 caused by the crystallographic phase transformation inducing an increase of the crystalline density of the
541 cobalt, leading to voids formation between particles. However, this porosity could not be explained by the
542 sole crystallographic phase transformation as it theoretically induces an aggregate density decrease of
543 20%, which is inferior to the decrease of 36% measured by ASAXS, or 54% measured by tomography.
544 Thermal stresses could thus be invoked in order to explain the high magnitude of porosity creation.
545 This structure change with the porosity increase during the reduction step appears to be very important as
546 it increases the “aggregate dispersion” (from 18% to 25%) and thus increases the number of accessible
547 cobalt active sites. The activity of the FT catalysts depending essentially on this number of accessible
548 metallic cobalt active sites, the optimization of the reduction step conditions in order to optimise the
549 creation of the porosity seems to be an interesting approach to improve the catalyst activity. Furthermore,
550 the FT catalyst selectivity is suspected to be sensitive to the proportion and size of the aggregates [8] that
551 are known to be controlled by the drying and calcination steps, hence to the active sites proximity. Once
552 again the aggregate structure and thus the reduction conditions could impact the selectivity. We can
553 suppose for example that varying the gas hourly space velocity, heating ramp, temperature, or the
554 pressure could lead to different aggregate structures.

556 **4 Conclusion**

557 In this study we have proposed a new approach that combines electron microscopy and ASAXS to
558 characterize Fischer-Tropsch cobalt-based catalysts in order to obtain a detailed and exhaustive
559 description of cobalt active phase. This last one is composed of dispersed nanoparticles and aggregates.
560 Analytical methodology and data treatment have been developed in ASAXS and electron tomography to
561 suit to these materials. Even if their principles are significantly different, ASAXS and electron
562 microscopy give information in term of particle and aggregate size in good agreement. Likewise, both
563 ASAXS and electron tomography provide some insight on the aggregate structure and morphology.

564 These complementary techniques have allowed in particular investigating the effect of the reduction step
565 on the particles and on the aggregates. We have shown that the reduction had a slight effect on the
566 particles, decreasing their mean size due to the crystallographic phase transformation from Co_3O_4 to Co^0 ,
567 but no phenomenon such as sintering has been observed. To the contrary, we have underlined that the
568 reduction has a significant effect on the aggregates of which morphology, size and structure are certainly
569 defined during the drying and calcination steps. The dense structure with few closed pores of the oxide
570 aggregates evolved into a polycrystalline, porous and airy structure. The porosity of the aggregates is
571 doubled which has the effect to increase drastically the dispersion inside the aggregates and thus increase
572 the number of accessible metallic cobalt active sites. Fischer-Tropsch catalysts activity and selectivity are
573 known to be sensitive to the number and the proximity of the active sites hence the aggregate structure
574 and porosity seem to be important parameters. The operating reduction conditions such as the gas hourly
575 space velocity or the temperature ramp are suspected to affect the internal thermal stresses and thus the
576 final aggregate structure and should be specifically investigated in order to try to improve the catalytic
577 properties.

578 Finally, as the reduction step has obviously a strong effect on the morphology, the structure and the
579 dispersion of the active phase, it appears clearly that the catalysts have to be characterize in their reduced
580 state in order to explain the catalytic performances. Moreover, it should be even more appropriate to
581 characterize the used catalyst after the catalytic test as the active phase and specially the aggregate
582 structure is potentially affected under Fischer-Tropsch conditions [45]. In this goal, the ASAXS technique
583 should be well suitable as it allows to characterize the particles and the aggregates simultaneously, but
584 especially on catalyst embedded in waxes produced by the synthesis and thus without carrying out a
585 specific washing apt to modify the sample.

586 This study opens prospects for understanding the role of the carrier chemical and textural properties on
587 the cobalt phase dispersion, but also the role of each drying, calcination and reduction unitary step on
588 particle and aggregates size distributions and cobalt phase dispersion, both parameters that control the
589 active sites number and proximity and thus the activity and the selectivity. Hence, confronting particles
590 and aggregates structure properties and the catalytic performances is the next step.

592 **5 Acknowledgements**

593 Electron tomography acquisitions were partially performed at «Centre Technologique des
594 Microstructures de l'Université Lyon I». The authors thank X. Jaurand for his support.

6 References

- [1] A.Y. Khodakov, W. Chu, P. Fongarland, Advances in the development of novel cobalt Fischer-Tropsch catalysts for synthesis of long-chain hydrocarbons and clean fuels, *Chemical reviews* 107 (2007) 1692–1744.
- [2] M.E. Dry, High quality diesel via the Fischer-Tropsch process - a review, *JOURNAL OF CHEMICAL TECHNOLOGY AND BIOTECHNOLOGY* 77 (2002) 43–50.
- [3] E.F. Sousa-Aguiar, F.B. Noronhac, Faro, Jr., Arnaldo, The main catalytic challenges in GTL (gas-to-liquids) processes, *CATALYSIS SCIENCE & TECHNOLOGY* 1 (2011) 698–713.
- [4] C. Bouchy, G. Hastoy, E. Guillon, J.A. Martens, Fischer-Tropsch Waxes Upgrading via Hydrocracking and Selective Hydroisomerization, *Oil & Gas Science and Technology - Rev. IFP* 64 (2009) 91–112.
- [5] J.P. den Breejen, P.B. Radstake, G.L. Bezemer, J.H. Bitter, V. Froseth, A. Holmen, K.P. de Jong, On the Origin of the Cobalt Particle Size Effects in Fischer-Tropsch Catalysis, *Journal of the American Chemical Society* 131 (2009) 7197–7203.
- [6] O. Borg, P.D.C. Dietzel, A.I. Spjelkavik, E.Z. Tveten, J.C. Walmsley, S. Diplas, S. Eri, A. Holmen, E. Ryttera, Fischer-Tropsch synthesis: Cobalt particle size and support effects on intrinsic activity and product distribution, *JOURNAL OF CATALYSIS* 259 (2008) 161–164.
- [7] J.-Y. Park, Y.-J. Lee, P.R. Karandikar, K.-W. Jun, K.-S. Ha, H.-G. Park, Fischer-Tropsch catalysts deposited with size-controlled Co₃O₄ nanocrystals: Effect of Co particle size on catalytic activity and stability, *APPLIED CATALYSIS A-GENERAL* 411 (2012) 15–23.
- [8] P. Munnik, P.E. de Jongh, K.P. de Jong, Control and Impact of the Nanoscale Distribution of Supported Cobalt Particles Used in Fischer-Tropsch Catalysis, *Journal of the American Chemical Society* 136 (2014) 7333–7340.
- [9] P. Munnik, N.A. Krans, P.E. de Jongh, K.P. de Jong, Effects of Drying Conditions on the Synthesis of Co/SiO₂ and Co/Al₂O₃ Fischer-Tropsch Catalysts, *ACS Catalysis* 4 (2014) 3219–3226.
- [10] L. Braconnier, E. Landrison, I. Clemencon, C. Legens, F. Diehl, Y. Schuurman, How does activation affect the cobalt crystallographic structure? An in situ XRD and magnetic study, *Catalysis Today* 215 (2013) 18–23.
- [11] Ø. Borg, J.C. Walmsley, R. Dehghan, B.S. Tanem, E.A. Blekkan, S. Eri, E. Rytter, A. Holmen, Electron Microscopy Study of γ -Al₂O₃ Supported Cobalt Fischer-Tropsch Synthesis Catalysts, *Catal Lett* 126 (2008) 224–230.

- 627 [12] S.W.T. Price, D.J. Martin, A.D. Parsons, W.A. Slawinski, A. Vamvakeros, S.J. Keylock, A.M.
628 Beale, J.F.W. Mosselmans, Chemical imaging of Fischer-Tropsch catalysts under operating
629 conditions, *SCIENCE ADVANCES* 3 (2017).
- 630 [13] H.-G. Haubold, K. Gruenhagen, M. Wagener, H. Jungbluth, H. Heer, A. Pfeil, H. Rongen, G.
631 Brandenberg, R. Moeller, J. Matzerath, P. Hiller, H. Halling, JUSIFA—A new user-dedicated
632 ASAXS beamline for materials science, *Rev. Sci. Instrum.* 60 (1989) 1943.
- 633 [14] H.-G. Haubold, X.H. Wang, ASAXS studies of carbon supported electrocatalysts, *Nuclear*
634 *Instruments and Methods in Physics Research Section B: Beam Interactions with Materials and*
635 *Atoms* 97 (1995) 50–54.
- 636 [15] H.-G. Haubold, X.H. Wang, H. Jungbluth, G. Goerigk, W. Schilling, In situ anomalous small-angle
637 X-ray scattering and X-ray absorption near-edge structure investigation of catalyst structures and
638 reactions, *Journal of Molecular Structure* 383 (1996) 283–289.
- 639 [16] H.G. Haubold, X.H. Wang, G. Goerigk, W. Schilling, In Situ Anomalous Small-Angle X-ray
640 Scattering Investigation of Carbon-Supported Electrocatalysts, *J Appl Crystallogr* 30 (1997) 653–
641 658.
- 642 [17] A. Benedetti, L. Bertoldo, P. Canton, G. Goerigk, F. Pinna, P. Riello, S. Polizzi, ASAXS study of
643 Au, Pd and Pd–Au catalysts supported on active carbon, *Catalysis Today* 49 (1999) 485–489.
- 644 [18] A. Benedetti, S. Polizzi, P. Riello, F. Pinna, G. Goerigk, ASAXS Investigation of a Au/C Catalyst,
645 *JOURNAL OF CATALYSIS* 171 (1997) 345–348.
- 646 [19] S. Polizzi, P. Riello, G. Goerigk, A. Benedetti, Quantitative investigations of supported metal
647 catalysts by ASAXS, *Journal of synchrotron radiation* 9 (2002) 65–70.
- 648 [20] G. Beaucage, H.K. Kammler, S.E. Pratsinis, Particle size distributions from small-angle scattering
649 using global scattering functions, *J Appl Crystallogr* 37 (2004) 523–535.
- 650 [21] P.A. Midgley, M. Weyland, 3D electron microscopy in the physical sciences: the development of Z-
651 contrast and EFTEM tomography, *Ultramicroscopy* 96 (2003) 413–431.
- 652 [22] O. Ersen, I. Florea, C. Hirlimann, C. Pham-Huu, Exploring nanomaterials with 3D electron
653 microscopy, *Materials Today* 18 (2015) 395–408.
- 654 [23] O. Ersen, C. Hirlimann, M. Drillon, J. Werckmann, F. Tihay, C. Pham-Huu, C. Crucifix, P. Schultz,
655 3D-TEM characterization of nanometric objects, *Solid State Sciences* 9 (2007) 1088–1098.
- 656 [24] A.H. Janssen, Van Der Voort, Pascal, A.J. Koster, de Jong, Krijn P., A 3D-TEM study of the shape
657 of mesopores in SBA-15 and modified SBA-15 materials Electronic supplementary information (ESI)
658 available: Fig. S1: schematic view of the MCM-41 formation mechanism. Movie S2: Aligned TEM
659 tilt series of the SBA-15 particle from Fig. 1 (sample with the lower TEOS to template ratio). Movie

660 S3: Aligned TEM tilt series of the SBA-15 particle from Fig. 3 (sample with the higher TEOS to
661 template ratio). See <http://www.rsc.org/suppdata/cc/b2/b204943k>, Chem. Commun. (2002) 1632–
662 1633.

663 [25] A.H. Janssen, A.J. Koster, de Jong, Krijn P., Three-Dimensional Transmission Electron Microscopic
664 Observations of Mesopores in Dealuminated Zeolite Y, *Angewandte Chemie International Edition*
665 40 (2001) 1102–1104.

666 [26] de Jong, Krijn P, J. Zečević, H. Friedrich, de Jongh, Petra E, M. Bulut, S. van Donk, R. Kenmogne,
667 A. Finiels, V. Hulea, F. Fajula, Zeolite Y crystals with trimodal porosity as ideal hydrocracking
668 catalysts, *Angewandte Chemie (International ed. in English)* 49 (2010) 10074–10078.

669 [27] J. Zečević, C.J. Gommès, H. Friedrich, de Jongh, Petra E, de Jong, Krijn P, Mesoporosity of zeolite
670 Y: quantitative three-dimensional study by image analysis of electron tomograms, *Angewandte*
671 *Chemie (International ed. in English)* 51 (2012) 4213–4217.

672 [28] J. Kenvin, S. Mitchell, M. Sterling, R. Warringham, T.C. Keller, P. Crivelli, J. Jagiello, J. Pérez-
673 Ramírez, Quantifying the Complex Pore Architecture of Hierarchical Faujasite Zeolites and the
674 Impact on Diffusion, *Adv. Funct. Mater.* 26 (2016) 5621–5630.

675 [29] J. Zečević, van der Eerden, Ad M.J., H. Friedrich, de Jongh, Petra E., de Jong, Krijn P., H₂PtCl₆-
676 derived Pt nanoparticles on USY zeolite: A qualitative and quantitative electron tomography study,
677 *Microporous and Mesoporous Materials* 164 (2012) 99–103.

678 [30] J. Zečević, van der Eerden, Ad M J, H. Friedrich, de Jongh, Petra E, de Jong, Krijn P,
679 Heterogeneities of the nanostructure of platinum/zeolite y catalysts revealed by electron tomography,
680 *ACS nano* 7 (2013) 3698–3705.

681 [31] L. Roiban, O. Ersen, C. Hirlimann, M. Drillon, A. Chaumonnot, L. Lemaitre, A.-S. Gay, L. Sorbier,
682 Three-Dimensional Analytical Surface Quantification of Heterogeneous Silica-Alumina Catalyst
683 Supports, *ChemCatChem* (2016) n/a-n/a.

684 [32] M.H. Gass, K.K.K. Koziol, A.H. Windle, P.A. Midgley, Four-dimensional spectral tomography of
685 carbonaceous nanocomposites, *Nano letters* 6 (2006) 376–379.

686 [33] J.C. Hernández-Garrido, K. Yoshida, P.L. Gai, E.D. Boyes, C.H. Christensen, P.A. Midgley, The
687 location of gold nanoparticles on titania, *Catalysis Today* 160 (2011) 165–169.

688 [34] P.D. Nellist, M.F. Chisholm, A.R. Lupini, A. Borisevich, W.H. Sides, S.J. Pennycook, N. Dellby, R.
689 Keyse, O.L. Krivanek, M.F. Murfitt, Z.S. Szilagy, Aberration-corrected STEM, *J. Phys.: Conf. Ser.*
690 26 (2006) 7–12.

- 691 [35] I. Arslan, J.C. Walmsley, E. Rytter, E. Bergene, P.A. Midgley, Toward three-dimensional
692 nanoengineering of heterogeneous catalysts, *Journal of the American Chemical Society* 130 (2008)
693 5716–5719.
- 694 [36] C.J. Gommers, G. Prieto, J. Zecevic, M. Vanhalle, B. Goderis, K.P. de Jong, P.E. de Jongh,
695 Mesoscale Characterization of Nanoparticles Distribution Using X-ray Scattering, *ANGEWANDTE*
696 *CHEMIE-INTERNATIONAL EDITION* 54 (2015) 11804–11808.
- 697 [37] J.R. Kremer, D.N. Mastrorade, J.R. McIntosh, Computer visualization of three-dimensional image
698 data using IMOD, *Journal of Structural Biology* 116 (1996) 71–76.
- 699 [38] D.N. Mastrorade, Dual-axis tomography: an approach with alignment methods that preserve
700 resolution, *Journal of Structural Biology* 120 (1997) 343–352.
- 701 [39] M. Moreaud, F. Cokelaer, FLOWING BILATERAL FILTER: DEFINITION AND
702 IMPLEMENTATIONS, *Image Anal Stereol* 34 (2015) 101.
- 703 [40] C.T. Chantler, Theoretical Form Factor, Attenuation, and Scattering Tabulation for $Z=1-92$ from
704 $E=1-10$ eV to $E=0.4-1.0$ MeV, *Journal of Physical and Chemical Reference Data* 24 (1995) 71–643.
- 705 [41] C.T. Chantler, Detailed Tabulation of Atomic Form Factors, Photoelectric Absorption and Scattering
706 Cross Section, and Mass Attenuation Coefficients in the Vicinity of Absorption Edges in the Soft X-
707 Ray ($Z=30-36$, $Z=60-89$, $E=0.1$ keV–10 keV), Addressing Convergence Issues of Earlier Work, *J.*
708 *Phys. Chem. Ref. Data* 29 (2000) 597.
- 709 [42] T. Binninger, M. Garganourakis, J. Han, A. Patru, E. Fabbri, O. Sereda, R. Kötz, A. Menzel, T.J.
710 Schmidt, Particle-Support Interferences in Small-Angle X-Ray Scattering from Supported-Catalyst
711 Materials, *Phys. Rev. Applied* 3 (2015).
- 712 [43] F. Zhang, J. Ilavsky, G.G. Long, Quintana, John P. G., A.J. Allen, P.R. Jemian, Glassy Carbon as an
713 Absolute Intensity Calibration Standard for Small-Angle Scattering, *Metall and Mat Trans A* 41
714 (2010) 1151–1158.
- 715 [44] C.S. Forbes, *Statistical distributions*, 4th ed., Wiley, Hoboken, N.J., 2011.
- 716 [45] D. Moodley, *On the deactivation of cobalt-based Fischer-Tropsch synthesis catalysts*, Technische
717 Universiteit Eindhoven, 2008.
- 718